PNAS
www.pnas.org

## Supplementary Information for manuscript entitled:

# *High Rac1 activity is functionally translated into cytosolic structures with unique nanoscale cytoskeletal architecture*

Daniel J. Marston[1], Karen L. Anderson[2], Mark F. Swift[2], Marie Rougie[1], Christopher Page[2], Klaus M. Hahn[1], Niels Volkmann[2*], Dorit Hanein[2*]

[1] Department of Pharmacology, The University of North Carolina at Chapel Hill, Chapel Hill, North Carolina, 27599, United States
[2] Bioinformatics and Structural Biology Program, Sanford Burnham Prebys Medical Discovery Institute, La Jolla, California, 92037, United States

Corresponding Authors: Niels Volkmann; Email: niels@burnham.org
Dorit Hanein; Email: dorit@burnham.org

**This PDF file includes:**

Material and Methods
Figures S1 to S8
Captions for movies S1 to S4
References for SI reference citations

**Other supplementary materials for this manuscript include:**

Movies S1 to S4


www.pnas.org/cgi/doi/10.1073/pnas.1808830116

## *Material and Methods*

### Rac1 GTPase biosensor and MEF cell culture:

The Rac1 FLARE DC1g biosensor is a modification of our previously reported dual chain biosensor design (1, 2). To improve brightness and dynamic range we used Turquoise fluorescent protein (3) rather than CyPet. In brief, YPet (4) is fused upstream of residues 57-142 of human PAK1, and Turquoise is fused to the N-terminus of full-length Rac1. The two biosensor chains were expressed on one open reading frame with two consecutive 2A viral peptide sequences from *Porcine teschovirus*-1 (P2A) and *Thosea asigna* virus (T2A) inserted between them, leading to cleavage of the two chains during translation (5). The biosensor constructs were inserted into a tet-off inducible retroviral expression system and stable lines were produced in tet-off MEFs (Mouse Embryonic Fibroblasts, Clontech). Cells were maintained in DMEM (Cellgro) with 10% FBS (Hyclone) and 0.2 µg/ml doxycycline to repress biosensor expression.

### Rac1 GTPase biosensor imaging:

Biosensor expression was induced in MEFs 48 hr prior to imaging through trypsinization and culturing without doxycycline. At 24 hr prior to imaging, the cells were replated on glass bottomed dishes (MatTek) with attached 200-mesh R5/20 holey carbon-coated gold finder grids (Quantifoil) that were coated with 5 µg/ml of bovine fibronectin (Sigma-Aldrich) at 37 °C overnight. Cells were imaged in Hams F-12(K) (Caisson Labs) with 5% FBS and 10 mM Hepes (Gibco). The markings on the finder grids were used to assign a unique number identifier for each cell for further CLEM processing.

Time-lapse images were acquired every 30 seconds on an Olympus IX81 inverted epifluorescence microscope fitted with temperature control (TC344, Warner Instruments). Cells were imaged using an Olympus 40x UPlan FLN 1.3 NA lens, and a TuCam imaging adapter (Andor) fitted with two HQ2 CCD cameras (Photometrics) to allow simultaneous capture of FRET and donor emission. Cells were illuminated with a 100 W Hg arc lamp through a neutral density 1.0 filter. For emission ratio imaging the following filter sets were used (Semrock): CFP: ex- FF-434/17, em- FF-482/35; FRET: ex- FF-434/17, em- FF-550/49; YFP: ex- FF-510/10, em- FF-550/49, using a dual band dichroic FF462/523.

### Rac1 GTPase biosensor image processing:

GTPase activation levels were measured in living cells by monitoring the ratio of FRET to donor emission on a pixel by pixel basis (6). Donor and FRET images were aligned using fluorescent beads as fiduciaries to produce a transformation matrix using the Matlab function “cp2tform” (Matlab, The Mathworks Inc.). This was then applied to the Donor image using the Matlab function “imtransform”.

The camera dark current was determined by obtaining images for each camera without excitation, and the dark current was subtracted from all images. Images were corrected for shading due to uneven illumination by taking images of a uniform dye solution under conditions used for each wavelength, normalizing this image to an average intensity of 1 to produce a reference image for each wavelength, and then dividing the images corrected for dark current by the shading correction reference image. Background fluorescence was removed by subtracting, at each frame, the intensity of a region containing no cells or debris. Images were segmented into binary masks with cell and non-cell regions using the segmentation package "MovThresh" (7), which is based on the Otsu algorithm (8). The Donor channel was used for segmentation, as it had the highest signal to noise ratio, particularly at the cell edge. The masks were then applied to all channels, setting non-cell regions to zero intensity. The masked images were corrected for bleed-through and ratios obtained using the following equation (using data from control cells expressing donor or acceptor alone to obtain the bleed-through coefficients α and β): $R = (FRET - \alpha(CFP) - \beta(YFP))/CFP$ where R is the Ratio, FRET is the total FRET intensity as measured, α is the bleed-through of the donor into the FRET signal, β is the bleed-through of acceptor into the FRET signal, and CFP and YFP are the donor and acceptor intensities as measured through direct excitation.

**Cryo-sample preparation and vitrification:**

Following the last live-cell image capture, cell movement was halted while maintaining the structural integrity of the site via rapid fixation. The cells were fixed in 2% formaldehyde, 0.1 M Pipes, 1 mM EGTA and 1 mM MgSO4 for 30 minutes at 37°C, washed in PHEM (60 mM Pipes, 25 mM Hepes, 2 mM MgSO4, 10 mM EGTA). The chemical reaction of the formaldehyde fixative typically reaches a depth of 5 mm in about 2 hours (9-11), which corresponds to full penetration of ~300 nm thick samples imaged here in less than 0.5 seconds. This value is nearly two orders of magnitude below the frame length of the life-cell imaging (30 seconds).

The fixed cells were manually plunge-frozen in liquid-nitrogen cooled liquefied ethane to prevent structural collapse or shrinkage associated with dehydration. The vitrification was done using a home-designed cryo-plunger.

**Cryo-light microscopy:**

The frozen grids were then mounted into grid support rings (Auto-gridTEM sample holder, FEI), and transferred to a cryo-light microscopy (cryo-LM) shuttle. Cryo-LM imaging was done using a CorrSight microscope equipped with a cryo-stage (ThermoFisher Scientific; FEI Company) operated at liquid nitrogen temperature. The cryo-LM allowed to verify the integrity of the samples after vitrification. In addition, the cryo-LM information was used to improve the precision of selecting regions of interest (specific heat signature in biosensor heat map) for cryo-tomography data collection (see below).

The CorrSight microscope includes a wide-field light path and a spinning disk confocal path with independent light sources. Z stacks of images were acquired using the MAPS data acquisition software (ThermoFisher Scientific; FEI company) on a 16-bit cooled CCD camera (Orca-Flash 4.0; Hamamatsu) using a set of air objective lenses. NA air objectives Zeiss Plan-ApoChromat 5x/0.16 NA and 20x/0.8 NA were used for obtaining overviews of the sample with transmitted light. Epifluorescence images were acquired using the Zeiss EC Plan-Neofluar 40x/0.9 NA Pol (working distance of 410 µm) air objective corrected for 170 µm cover glass thickness. Z stacks were acquired at increments of 1 µm at 40X, and a maximum intensity projection of the z-stack was calculated to flatten out variations of the focal plane. The fluorescence intensities were corrected by background subtraction.

**Correlative cryo-light and cryo-electron microscopy:**

For correlative cryo-light-electron microscopy (cryo-CLEM), the same cryo-grids were transferred after cryo-LM data collection from the CorrSight into a Titan Krios cryo-electron microscope (ThermoFisher Scientific, FEI Company). An overview image (atlas) of the entire grid was acquired to identify cells with fluorescence signal using the finder markings on the grids, which are visible in all three imaging modalities. Low-resolution images of the grid squares (pixel size 14-28 nm) containing the identified cells were acquired to allow alignment of LM, cryo-LM and cryo-tomography images of the same cell (see below).

**Cellular cryo-tomography:**

Electron cryo-tomography data was taken with an FEI Titan Krios equipped with an extra-high brightness field emission gun (XFEG) and operated at 300 kV. Tilt series (±65°, every 1.5°) were acquired on the back-thinned 4k × 4k FEI Falcon II direct detection imaging device under minimal dose conditions using the Tomo package in batch mode (ThermoFisher Scientific; FEI Company) at an average dose of about 100-120 $e^-/Å^2$ and defocus of 8-15 µm. Magnification was chosen to result in pixel sizes of 0.25 and 0.5 nm in the reconstructions. The fidelity and quality of the data collection was monitored with real-time automatic reconstruction protocols implemented in the pyCoAn package, an extended python version of the CoAn package (12). Five to fifteen consecutive tomograms from single cells were acquired, for a total of 171 tomograms from 25 cells. The correspondences between actin filament organization and Rac1 activity were fully consistent over all cells and cryo-tomograms investigated. Statistical analyses using parametric (t-test) as well as non-parametric (Mann-Whitney and Kolmogorov-Smirnov) all indicate that the difference of the two actin organizations in low and high Rac1 activity regions is statistically significant at a p-value $p<0.0001$.

**Image reconstruction and post-processing:**

Tilt series were aligned using the IMOD package (13) with a combination of fiducial-based and patch-based approaches. Three- dimensional densities were generated using the Simultaneous Iterative Reconstruction Technique (SIRT) as implemented in Tomo3D (14). This reconstruction technique tends to show a better definition of actin filaments as well as cell membranes than alternative Fourier or weighted back-projection methods. Reconstructions were binned by a factor of two for further analysis. Non-local means filtering (15) was applied to reduce noise for visualization. All processing was performed on the unfiltered reconstructions.

**Alignment of biosensor fluorescence and cryo-EM data:**

Low-magnification cryo-EM images where aligned with the cryo-LM images and the biosensor heat maps using the holes in the carbon (16). These are visible and well defined in all three imaging modalities and their centers can be determined with high accuracy. The estimated accuracy for the alignment of the biosensor heat maps to the low-magnification cryo-EM images based on the prediction error (16) was 82.7 ± 6.7 nm. The tomogram regions were located and aligned to the low-magnification images using a Z-projection image of the final tomogram and correlation-based template matching. The inverse transformation was then applied to the aligned cryo-LM and biosensor heat maps, allowing accurate correlation of features in the tomograms with heat signatures of the biosensor heat maps.

**Feature detection and sub-tomogram averaging:**

Actin filaments ribosomes and TRP-1 ring complexes were automatically detected and quantified using reduced representation templates as described previously (17). Cell membranes were traced using a semi-automatic graph cut approach (18). Tentative ribosomes picked automatically from regions with low Rac1 activity were cut out to provide an estimate for the resolution of the tomographic reconstructions using sub-tomogram averaging. We used iterative rounds of wedge-weighted correlation (19), as implemented in pyCoAn, with a starting model calculated from a human 80S ribosome single particle reconstruction (20), filtered to 10 nm resolution to remove model bias. The average of the aligned particles served as starting model for the next iteration. For each round, aligned particles with correlations smaller than 3σ below the mean were considered outliers and removed before calculating the average. The removed particles were added back for the next iteration. The iteration process was terminated when the correlation between averages of successive rounds exceeded 99.9% (5 rounds). 2098 particles contributed to the final average. The resolution was estimated by calculating a Fourier shell correlation between the final average and the 80S single particle reconstruction. The 0.33 cut-off criterion, recently proposed as an appropriate cut-off in a similar context (21), yielded a resolution estimate of 3.2 nm. The more conservative 0.5 cutoff criterion yielded a resolution estimate of 4.0 nm.

To investigate whether there is potential clustering of ribosomes, an analysis on nearest neighbor distances (22) was performed. Only distances below 54 nm were considered for this calculation.

Selected, automatically detected tentative TRP-1 ring complexes were compared to the high-resolution structure (23) using structure fitting with wedge-weighted correlation. Surface representations were generated using Chimera (24), and micrograph and tomography slice images were generated using IMOD (13).

## *Figures:*

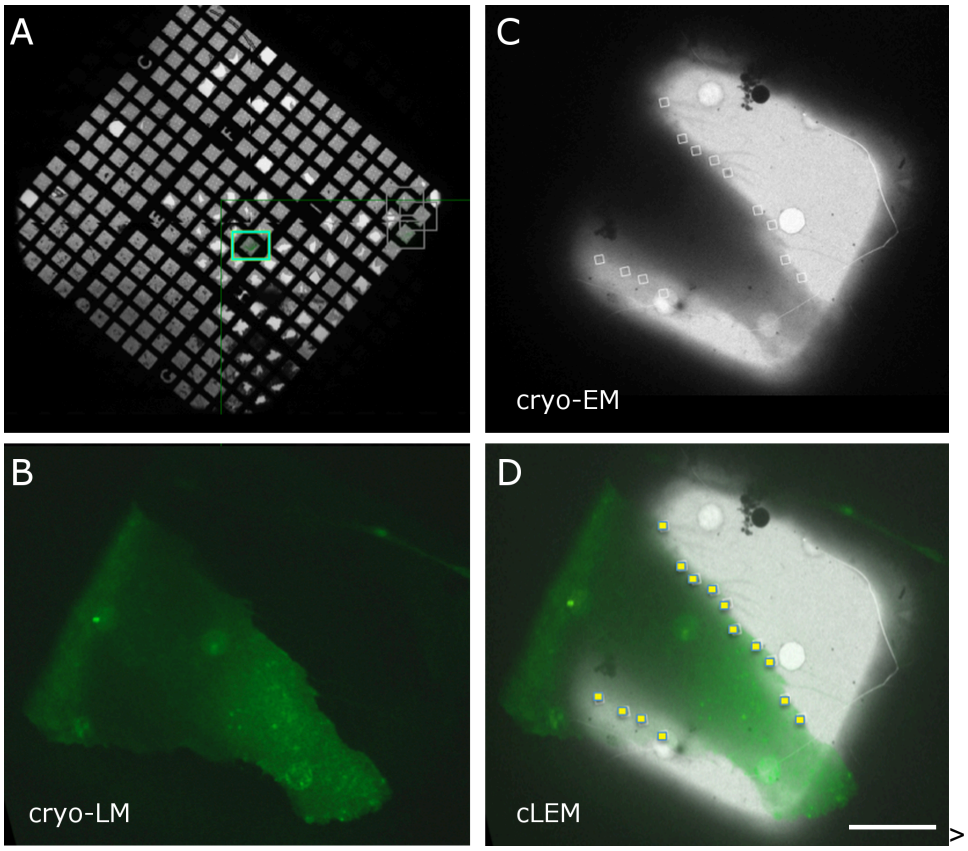


***Figure S1: Workflow tying live cell imaging to cryo-imaging modalities.*** (A) Overview of electron microscopy grid after loading into the CorrSight cryo light microscope. (B) Cryo fluorescence image of cell with Rac1 biosensor. This step allows to locate the fluorescing cell on the EM grid and provides an additional point for the correlation procedure after plunge freezing. (C) Electron cryo-microscopy overview image of the same cell (D) Overlay of the two images, regions marked for cryo-tomography marked by boxes. Bar is 20 microns.

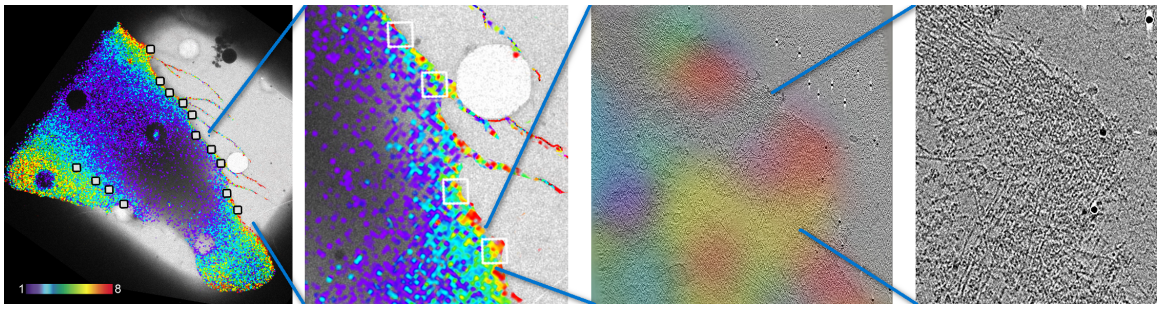


**Figure S2:** ***Correlative imaging – Scale integration****.* The last frame of the live-cell Rac1 activity imaging (left) can be linked to the nanoscale 3D morphology obtained by electron cryo-tomography (right) by successively traversing through scales. The pseudocolor scale shows the increase in ratio relative to the lowest 5% of ratio values in the cell. Low Rac1 activity corresponds to purple and blue areas, high Rac1 activity corresponds to red areas.

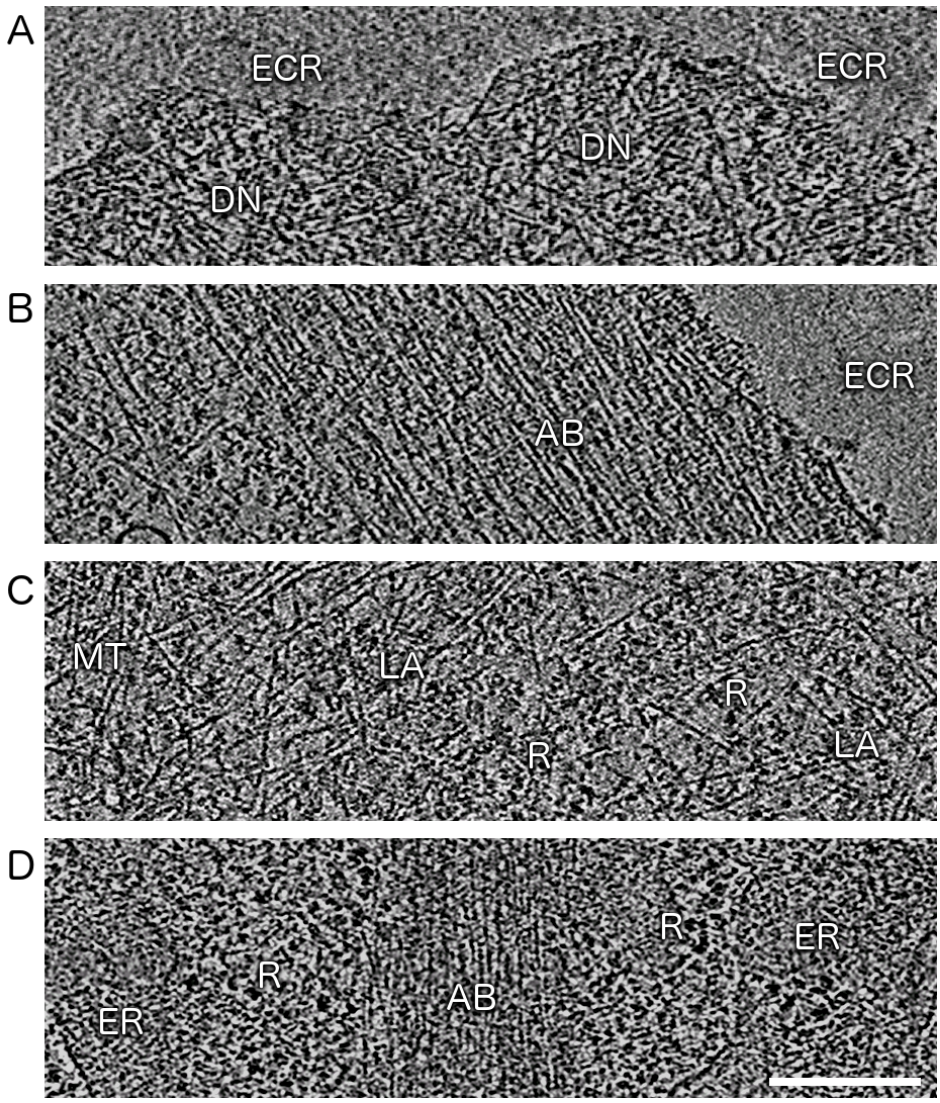


**Figure S3:** ***Different types of actin filament organizations found in MEF cells.*** 20-nm thick slices through 3D volumes of tomographic reconstructions are shown. (A) Dendritic network (DN) adjacent to the cell periphery (top). Actin filaments appear as dark line-like features. Actin branches are visible, most likely mediated by Arp2/3 complex, where smaller filaments branch off longer filaments at an approximate angle of 80º. ECR denotes extra cellular region. (B) Bundles of long actin filaments (AB) running parallel to the cell periphery (to the right). (C) Loosely arranged long actin filaments (LA) interspersed with macromolecular complexes such as ribosomes (dark spot-like features; R) and microtubules (MT). (D) Bundles of long actin filaments (AB) further away from the cell periphery (more than two microns) surrounded by other cellular features such as ribosomes (R) and endoplasmic reticulum (ER). The bar is 300 nm.

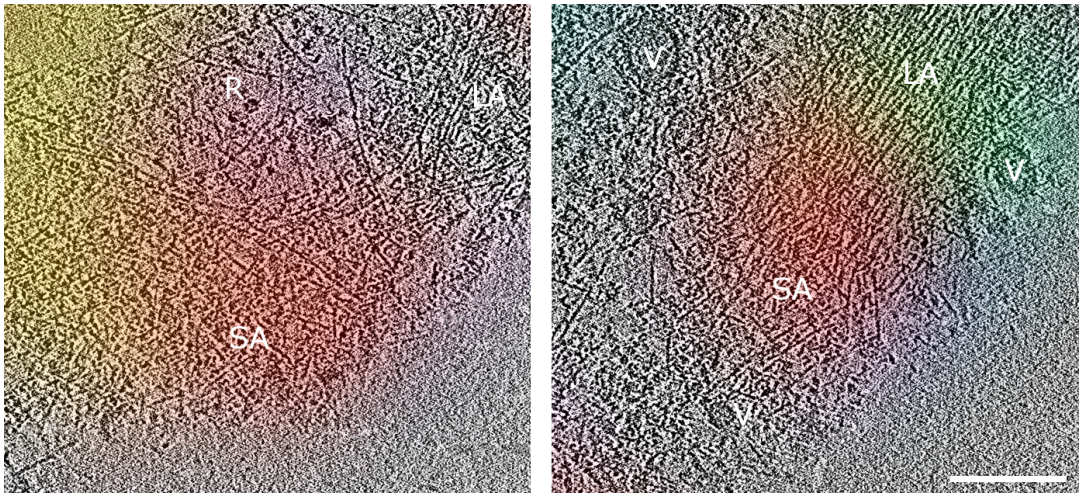


**Figure S4:** ***The macromolecular organization of cytoskeleton assemblies at regions of high Rac1 activity.*** 20-nm thick slices through regions with high activity (red) of Rac1 show high densities of short actin filaments (SA). Features that are typically observed in high numbers within regions of low Rac1 activity such as ribosomes (R), long actin filaments (LA), or vesicles (V) are rare in regions with high Rac1 activity and tend to be outside the red regions. Bar is 300 nm.

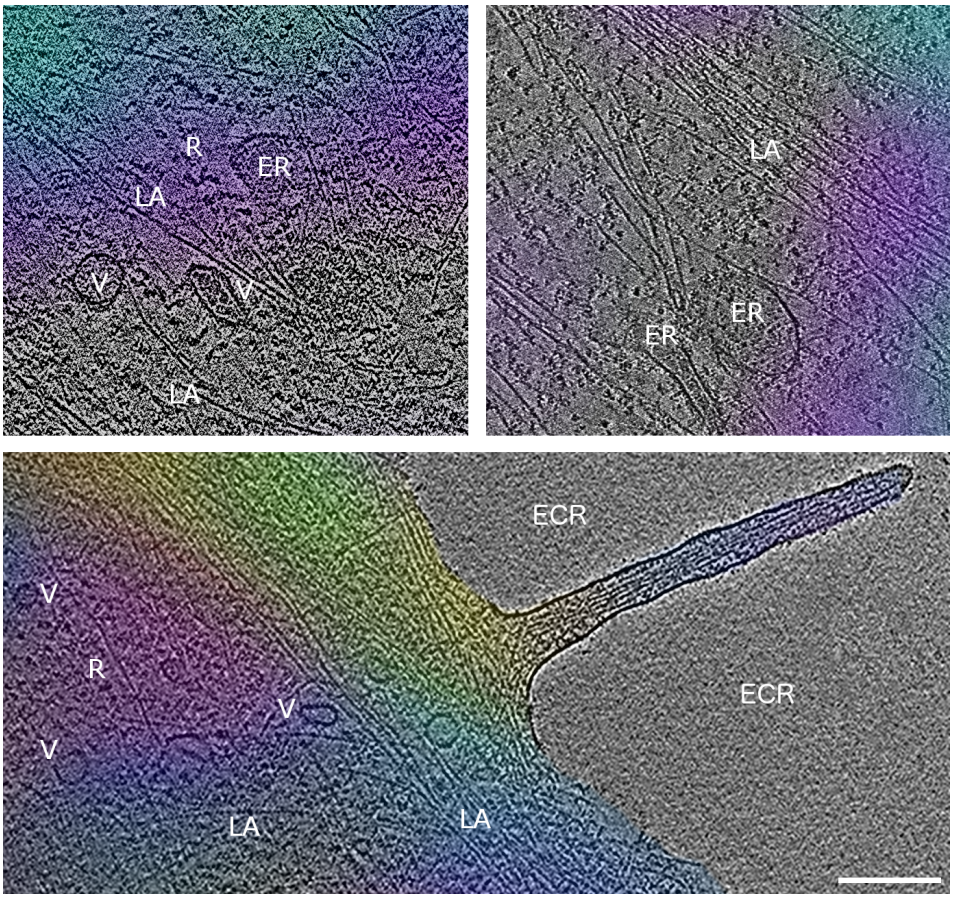


**Figure S5:** ***The Nanometer-scale organization of cytoskeleton assemblies at regions with low Rac1 activity.*** 20-nm thick slices through regions with low Rac1 activity (purple, blue) contain long actin filaments (LA), various types of vesicles (V), ribosomes (R), and endoplasmic reticulum (ER). ECR denotes extra cellular region. Bar is 300 nm.

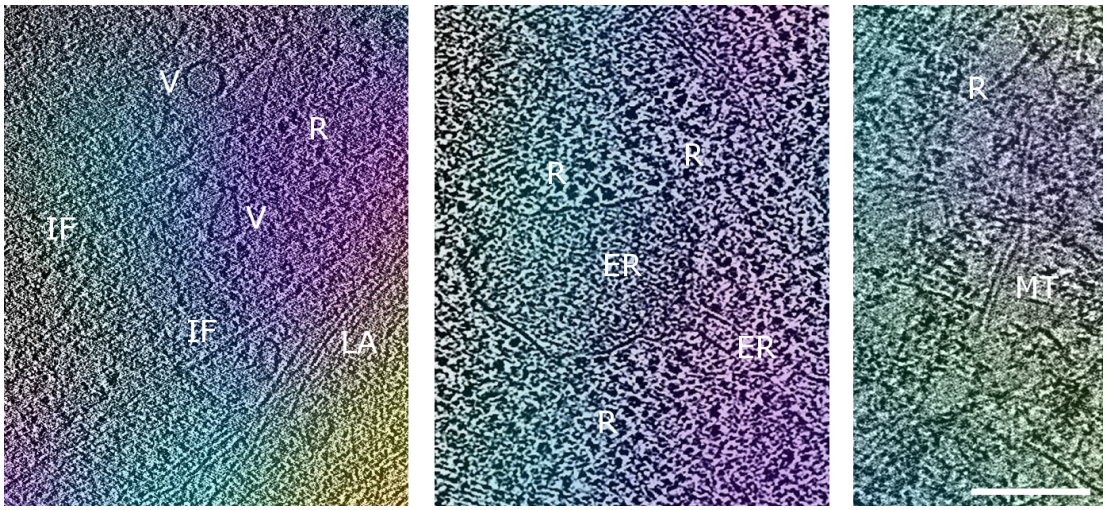


**Figure S6:** ***The Nanometer-scale organization cytoskeleton assemblies at regions with low Rac1 activity.*** 20-nm thick slices through regions with low activity (purple, blue) of Rac1 also contain intermediate filaments (IF), microtubules (MT) and dense ribosome (R) patches interspersed with endoplasmic reticulum (ER). Bar is 300 nm.

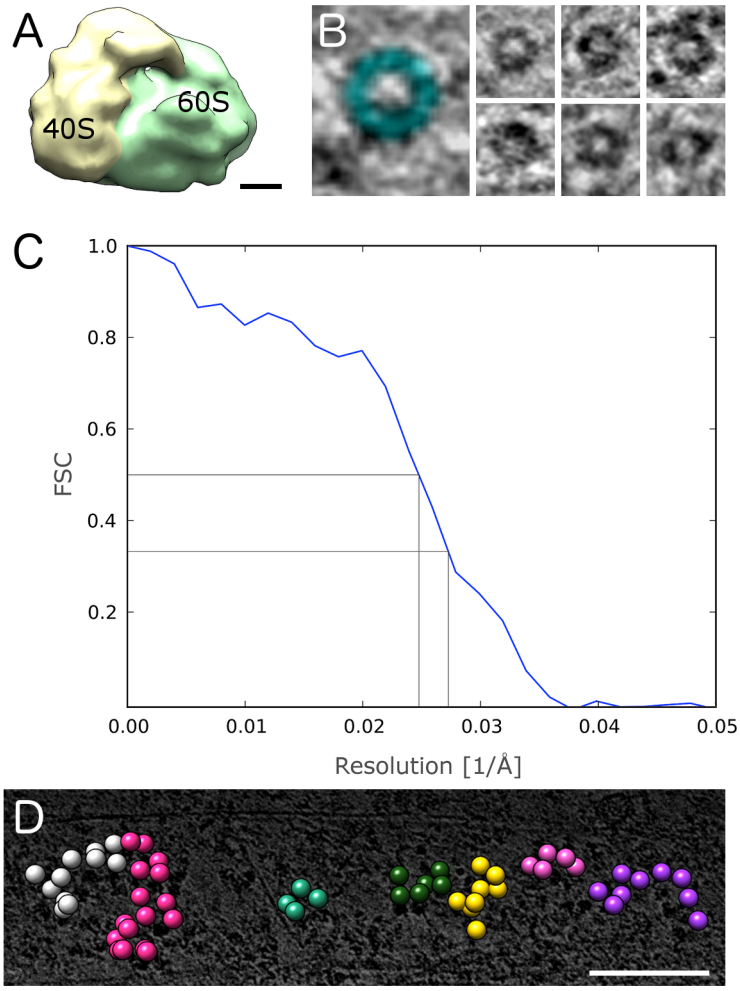


**Figure S7:** ***Resolution estimation***. (A) Sub-tomogram average of 2098 identified 80S ribosomes in regions of low Rac1 activity. (D) Slices through tentative TCP-1 Ring Complex chaperonins in regions of low Rac1 activity. The cyan overlay corresponds to density calculated at 3.5 nm resolution from the fitted atomic model of Saccharomyces cerevisiae TCP-1 Ring Complex. Width of the boxes is 23 nm. (C) Fourier Shell Correlation (FSC) between sub-tomogram average shown in A and a single particle reconstruction of the human 80S ribosome. The 0.33 cut-off criterion, recently proposed as an appropriate cut-off in a similar context (21), yielded a resolution of 3.2 nm. The more conservative 0.5 cutoff criterion yielded a resolution of 4.0 nm. (D) Representative ribosome clusters in a region of low Rac1 activity. Bar is 200 nm

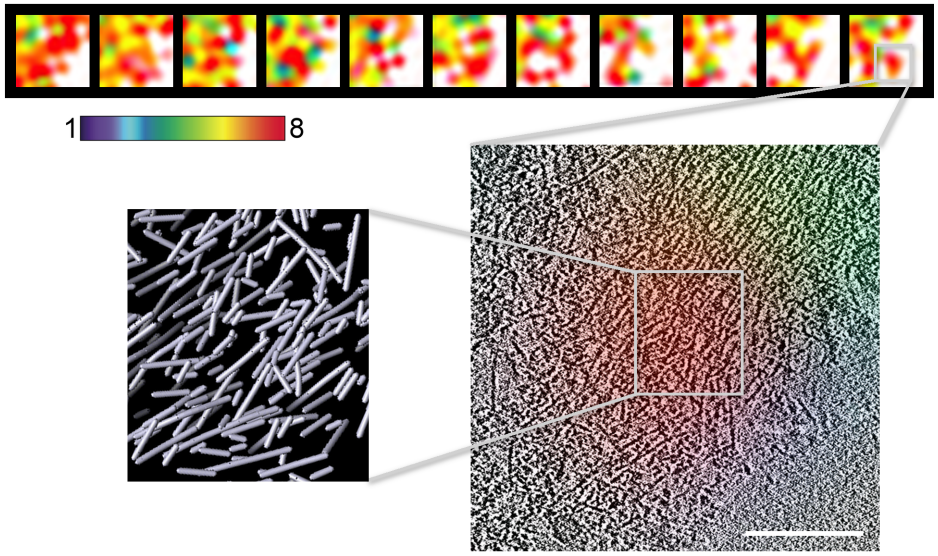


**Figure S8:** ***Correlating time evolution with molecular organization of cytoskeleton assemblies in regions of high Rac1 activity.*** In regions where high Rac1 activity persists over several minutes, short actin filaments are observed. The upper row shows time points of the same region every 30 seconds. The pseudocolor scale shows the increase in ratio relative to the lowest 5% of ratio values in the cell. The lower panel shows a 20 nm slice through a cryo-ET reconstruction recorded at the final time point of the activity imaging series. Bar is 300 nm.

## *Movies*

**Movies S1:** Example (1) of time-series of Rac1 GTPase activity evolution

**Movies S2:** Example (2) of time-series of Rac1 GTPase activity evolution

**Movie S3:** Successive slices through cryo-ET reconstruction of region with high Rac1 activity showing short, actin filaments with little mutual alignment in the red region (highest Rac1 activity).

**Movie S4:** Successive slices through cryo-ET reconstruction of region with low Rac1 activity showing long mutually aligned actin filaments, ribosomes, intermediate filaments, and vesicular structures.

## References


1. Machacek M*, et al.* (2009) Coordination of Rho GTPase activities during cell protrusion. *Nature* 461(7260):99-103.
2. Kraynov VS*, et al.* (2000) Localized rac activation dynamics visualized in living cells. *Science* 290:333-337.
3. Markwardt ML*, et al.* (2011) An improved cerulean fluorescent protein with enhanced brightness and reduced reversible photoswitching. *PLoS One* 6(3):e17896.
4. Nguyen AW & Daugherty PS (2005) Evolutionary optimization of fluorescent proteins for intracellular FRET. *Nat Biotechnol*.
5. Kim JH*, et al.* (2011) High Cleavage Efficiency of a 2A Peptide Derived from Porcine Teschovirus-1 in Human Cell Lines, Zebrafish and Mice. *Plos One* 6(4).
6. Hodgson L, Shen F, & Hahn K (2010) Biosensors for characterizing the dynamics of rho family GTPases in living cells. *Curr Protoc Cell Biol* Chapter 14:Unit 14 11 11-26.
7. Tsygankov D*, et al.* (2014) CellGeo: a computational platform for the analysis of shape changes in cells with complex geometries. *J Cell Biol* 204(3):443-460.
8. Otsu N (1979) Threshold Selection Method from Gray-Level Histograms. *Ieee T Syst Man Cyb* 9(1):62-66.
9. Baker JR (1958) *Principles of biological microtechnique; a study of fixation and dyeing* (Methuen; Wiley, London, New York,) p 357 p.
10. Dempster WT (1960) Rates of penetration of fixing fluids. *Am J Anat* 107:59-72.
11. Kiernan JA (2000) Formaldehyde, formalin, paraformaldehyde and glutaraldehyde: What they are and what they do. *Microscopy Today* 00(1):8-12.
12. Volkmann N & Hanein D (1999) Quantitative fitting of atomic models into observed densities derived by electron microscopy. *J Struct Biol* 125(2-3):176-184.
13. Kremer JR, Mastronarde DN, & McIntosh JR (1996) Computer visualization of three-dimensional image data using IMOD. *J Struct Biol* 116(1):71-76.
14. Agulleiro JI & Fernandez JJ (2011) Fast tomographic reconstruction on multicore computers. *Bioinformatics* 27(4):582-583.
15. Buades A, Coll B, & Morel JM (2005) A non-local algorithm for image denoising. *Proc Cvpr Ieee*:60-65.
16. Anderson KL, Page C, Swift MF, Hanein D, & Volkmann N (2018) Marker-free method for accurate alignment between correlated light, cryo-light, and electron cryo-microscopy data using sample support features. *J Struct Biol* 201(1):46-51.
17. Xu XP, Page C, & Volkmann N (2015) Efficient Extraction of Macromolecular Complexes from Electron Tomograms Based on Reduced Representation Templates. *Lect Notes Comput Sc* 9256:423-431.

18. Rother C, Kolmogorov V, & Blake A (2004) "GrabCut" - Interactive foreground extraction using iterated graph cuts. *Acm T Graphic* 23(3):309-314.

19. Volkmann N (2010) Methods for Segmentation and Interpretation of Electron Tomographic Reconstructions. *Method Enzymol* 483:31-46.

20. Spahn CM*, et al.* (2004) Cryo-EM visualization of a viral internal ribosome entry site bound to human ribosomes: the IRES functions as an RNA-based translation factor. *Cell* 118(4):465-475.

21. Mahamid J*, et al.* (2016) Visualizing the molecular sociology at the HeLa cell nuclear periphery. *Science* 351(6276):969-972.

22. Brandt F, Carlson LA, Hartl FU, Baumeister W, & Grunewald K (2010) The three-dimensional organization of polyribosomes in intact human cells. *Mol Cell* 39(4):560-569.

23. Zang Y*, et al.* (2016) Staggered ATP binding mechanism of eukaryotic chaperonin TRiC (CCT) revealed through high-resolution cryo-EM. *Nat Struct Mol Biol* 23(12):1083-1091.

24. Goddard TD, Huang CC, & Ferrin TE (2007) Visualizing density maps with UCSF Chimera. *Journal of Structural Biology* 157(1):281-287.